Mon. Not. R. Astron. Soc. **000**, 1–13 (0000) Printed 14 December 2010 (MN LATEX style file v2.2)

The LBA Calibrator Survey of southern compact extragalactic radio sources — LCS1

Leonid Petrov[1⋆], Chris Phillips[2], Alessandra Bertarini[3], Tara Murphy[4,5], and Elaine M. Sadler[4]

[1] *ADNET Systems, Inc./NASA GSFC, Code 610.2, Greenbelt, MD 20771 USA*
[2] *CSIRO Astronomy and Space Science, PO Box 76, Epping, NSW 1710, Australia*
[3] *Institute of Geodesy and Geoinformation, University of Bonn, Nussallee 17, Bonn, Germany and Max Planck Institute for Radioastronomy, Bonn, Germany*
[4] *Sydney Institute for Astronomy, School of Physics, The University of Sydney, NSW 2006, Australia*
[5] *School of Information Technologies, The University of Sydney, NSW 2006, Australia*

14 December 2010

ABSTRACT

We present a catalogue of positions and correlated flux densities of 410 flat-spectrum, compact extragalactic radio sources, previously detected in the AT20G survey. The catalogue spans the declination range $[-90°, -40°]$ and was constructed from four 24 hour VLBI observing sessions with the Australian Long Baseline Array made at 8.3 GHz. The detection rate in these experiments is 97%. The median uncertainty of source positions is 2.6 mas, the median correlated flux density at baseline projections lengths longer than 1000 km is 0.14 Jy. The goal of this work is 1) to provide a pool of sources with positions known at the milliarcsecond level of accuracy that are needed for phase referencing observations, for geodetic VLBI, and for space navigation; 2) to extend the complete flux-limited sample of compact extragalactic sources to the southern hemisphere; and 3) to investigate parsec-scale properties of high-frequency selected sources from the AT20G survey. As a result of the campaign, the number of compact radio sources with declinations $< -40°$ detectable with VLBI with measured correlated flux densities and positions known with the milliarcsec level of accuracies increased by a factor of 3.5. The catalogue and supporting material is available at `http://astrogeo.org/lcs1`.

Key words: astrometry – catalogues – instrumentation: interferometers – radio continuum – surveys

1 INTRODUCTION

Catalogues of positions of compact extragalactic radio sources with the highest accuracy are important for many applications. Among of them are imaging faint radio sources in the phase referencing mode, differential astrometry, space geodesy, and space navigation. The method of VLBI first proposed by Matveenko, Kardashev & Sholomitskii (1965) allows us to derive the position of sources with nanoradian precision (1 nrad $\approx$ 0.2 mas). The first catalogue of source coordinates determined with VLBI contained 35 objects (Cohen & Shaffer 1971). Since then hundreds of sources have been observed under geodesy and astrometry VLBI observing programs at 8.6 and 2.3 GHz (X and S bands) using the Mark3 recording system at the International VLBI Service for Geodesy and Astrometry (IVS) network. Analysis of these observations resulted in the ICRF catalogue of 608 sources (Ma et al. 1998). Later, using the very long baseline array (VLBA), positions of 4000 compact radio sources were determined in the framework of the VLBA Calibrator Survey (VCS) (Beasley et al. 2002; Fomalont et al. 2003; Petrov et al. 2005, 2006; Kovalev et al. 2007; Petrov et al. 2007a) and the geodetic program RDV (Petrov et al. 2009b). All sources with declinations above $-45°$ detected using Mark3/Mark4 under IVS programs were re-observed with the VLBA under VCS and RDV programs, which significantly improved the accuracy of their positions. As a result of these efforts, the probability of finding a calibrator with a VLBI-determined position greatly increased. In the declination range $\delta > -30°$ the probability of finding a calibrator within a 3° radius of a given position reached 97% by 2008.

⋆ E-mail:Leonid.Petrov@lpetov.net

© 0000 RAS

However, the VLBA is located in the northern hemisphere. Observations in the declination zone $[-50°, -30°]$ are difficult, and the array does not see sources with $\delta < -52°$. In 2008, the probability of finding a calibrator within a radius of 3° was 75% in the declination zone $[-40°, -30°]$ and only 42% for declinations $< -40°$. In 2008 the VLBI calibrator list[1] had 524 sources in the zone $[+52°, +90°]$ and only 98 objects in the zone $[-52°, -90°]$, unreachable to the VLBA. These southern sources were observed during geodetic experiments and during two dedicated southern hemisphere astrometry campaigns (Fey et al. 2004, 2006).

The reason for this disparity is the scarcity of VLBI antennas in the southern hemisphere, particularly stations with dual frequency S/X receivers and geodetic recording systems. Also until recently there has been a lack of good all-sky catalogs suitable as candidate VLBI calibrators. The Australian Long Baseline Array (LBA) consists of six antennas located in Australia with the South Africa station HARTRAO often joining in. The VLBI networks observes 3–4 sessions a year of about one week long each. Although the hardware used by the LBA was not designed for geodesy and absolute astrometry observations, it was demonstrated by Petrov et al. (2009a) that despite significant technical challenges, absolute astrometry VLBI observations with the LBA network is feasible. In a pilot experiment in June 2007 positions of participating stations were determined with accuracies 3–30 mm, and positions of 5 new sources were determined with accuracies 2–5 mas.

Inspired by these astrometric results, we launched the X-band LBA Calibrator Survey observing campaign (LCS), with the aim of determining milliarcsecond positions and correlated flux densities of one thousand compact extragalactic radio sources with declinations $< -30°$. The overall objective of this campaign is to match the density of calibrators in the northern hemisphere and to eliminate the disparity.

We pursue three long-term goals of this campaign. First, a dense grid of calibrators with precisely known positions within several degrees of any target makes feasible phase-referencing observations of weak targets. According to Wrobel (2009), during 2003–2008 63% of VLBA observations were made in the phase referencing mode. A dense grid of calibrators also makes possible differential astrometry of galactic objects, such as pulsars and masers, and it allows direct determination of the parallax at distances up to several kiloparsec (Deller et al. 2009). These sources form the pools of targets for observations under geodesy program and for space navigation.

The second goal is to extend the complete flux-limited sample of compact extragalactic radio sources with emissions from milliarcsecond-size regions to the entire sky. According to Kovalev (private communication, 2010), analysis of the $\log N$–$\log S$ diagram of the VLBI calibrator list suggests the sample of radio loud Active Galaxy Nuclei (AGN) is complete at the level of 200 mJy of the correlated flux density at X-band at spatial frequencies 25 $M\lambda$ in the zone with $\delta > -30°$. Extending the complete sample to the entire sky will make it possible to generalize the properties of the sample, such as distribution of compactness, distribution of brightness temperature, bulk motion, viewing angle, irregularities of the spatial distribution and some others, to the entire population of radio loud AGN.

The third goal was to investigate properties of high-frequency selected radio sources from Australia Telescope 20 GHz (AT20G) survey (Murphy et al. 2010; Massardi et al. 2010). Obtaining observations of a subsample of AT20G sources with milliarcsecond resolution will allow us to investigate properties, such as spectral index, polarization fraction and variability, of a population of extremely compact sources.

In this paper we present the results from the first four 24-hour experiments that were observed in 2008–2009. Selection of candidate sources based on the AT20G catalogue is discussed in section 2. The station setups during the observing sessions is described in section 3. Correlation and post-correlation analysis which is rather different from ordinary VLBI experiments is discussed in section 4 and 5. Errors analysis of single-band observations, including evaluation of ionosphere-driven systematic errors, is given in subsection 5.2. The catalogue of source positions and correlated flux densities is presented in section 6. The results are summarized in section 7.

2 CANDIDATE SOURCE SELECTION

The AT20G is a blind radio survey observed at 20 GHz with the Australia Telescope Compact Array (ATCA) between 2004 and 2008 (Murphy et al. 2010). It covers the whole sky south of declination 0°. The source catalogue is an order of magnitude larger than previous catalogues of high-frequency radio sources, with 5890 sources above a 20 GHz flux-density limit of 40 mJy. All AT20G sources have total intensity and polarization measured at 20 GHz, and most sources south of declination −15° also have near-simultaneous flux-density measurements at 4.8 and 8.6 GHz. A total of 1559 sources were detected in polarised total intensity at one or more of the three frequencies. There are also optical identifications and redshifts for a significant fraction of the catalogue.

This high-frequency catalogue provides a good starting point for selecting bright, compact sources and candidate calibrators. Massardi et al. (2010) show that almost all the flat-spectrum AT20G sources with spectral index $\alpha > -0.5$ are unresolved on scales of 0.1–0.2 arcsec in size at 20 GHz (see their Figure 3.4). The few exceptions are either (i) foreground Galactic and LMC sources such as planetary nebulae, HII regions and pulsar wind nebulae, which have a flat radio spectrum due to their thermal emission but are usually resolved on scales of a few arcsec (Murphy et al. 2010), or (ii) flat-spectrum extragalactic sources which are gravitationally-lensed, like PKS 1830−211.

For 64% of sources from the AT20G catalogue, flux densities were determined in three bands, 5.0, 8.4 and 20 GHz. We used these measurements to calculate the spectral index α ($F \sim f^{\alpha}$). We selected a set of 684 objects, previously not observed with VLBI with a flux density > 150 mJy at 8.3 GHz and with spectral index > -0.6. We then split this sample into two subsets: 410 high priority sources with flux densities > 200 mJy and spectral indices > -0.5, and all others. In addition, we selected 14 flat-spectrum objects that did not have flux density measurements at 5 GHz and

[1] Available at `http://astrogeo.org/rfc`

Table 1. The LBA network stations. The average System Equivalent Flux Density (SEFD) at 8.3 GHz at elevation angles $> 60°$ achieved in LCS1 experiments shown in the last column.

Name	ϕ_{gc}	λ	Diam	SEFD
ATCA-104	-30°.15	149°.57	20 m	350 Jy
CEDUNA	-31°.70	133°.81	32 m	490 Jy
DSS45	-35°.22	148°.98	34 m	120 Jy
HOBART26	-42°.62	147°.44	26 m	620 Jy
MOPRA	-31°.10	149°.10	22 m	380 Jy
PARKES	-32°.82	148°.26	64 m	36 Jy

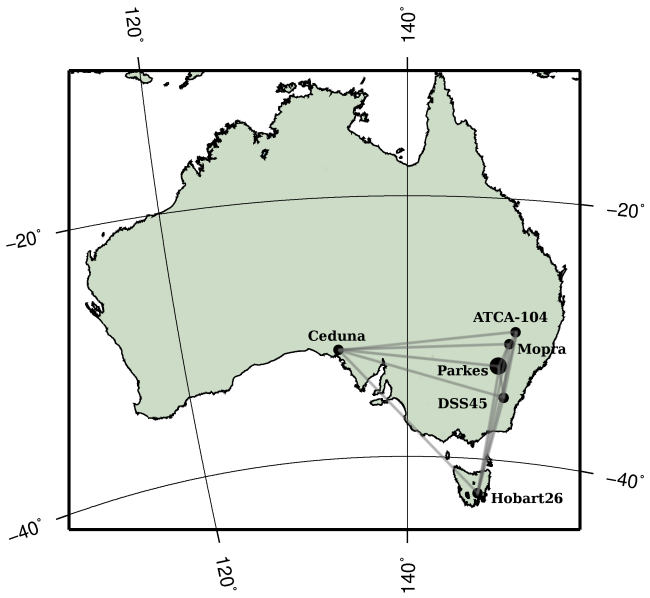

Figure 1. The LBA network used for LCS1 observations.

8 GHz in AT20G. Their spectral indices were determined by analyzing historical single dish observations found in the Astrophysical CATalogs support System CATS (Verkhodanov et al. 1997) — the database that currently includes catalogues from 215 radioastronomy surveys.

In addition to target sources, we identified a set of 195 sources that we used for calibrator selection. These were bright sources previously observed at the VLBA or IVS network with position known with accuracies better 0.5 mas and with correlated flux densities > 500 mJy on baselines longer than 5000 km.

2.1 The Long Baseline Array

The LBA network used for LCS1 consists of 6 stations: ATCA-104, CEDUNA, DSS45, HOBART26, MOPRA and PARKES (Figure 1, Table 1). The maximum baseline length of the network is 1703 km, the maximum equatorial baseline projection is 1501 km, and the maximum polar baseline projection is 963 km.

2.2 Observation scheduling

Observation schedules were prepared with the software program sur_sked. The scheduling goal was to observe each target source at all antennas of the array in 3 scans of 120 seconds each in the first three experiments and in 4 scans in the last experiment. After tracking a target source for 120 seconds, each antenna immediately slewed to the next object. The minimum time interval between consecutive scans of the same source was 3 hours. The scheduling software computed elevation and azimuths of candidate sources with constraints on the horizon mask and maximum elevations to which antennas can point. It calculated the slewing time taking into account the antenna slewing rate, slewing acceleration and cable wrap constraints. The sources were scheduled in the sequence that minimizes slewing time and fits scheduling constraints. A score was assigned for each target source visible at a given time. The score depends on the slewing time, the history of past observations in the experiment and the amount of time that the source will remain visible to all antennas in the array.

Every hour a set of 4 calibrator sources was observed: two scans with all antennas with their elevation in the range $[12°, 45°]$, one scan at elevations $[32°, 45°]$ and one scan at elevations $[45°, 90°]$. Scans with calibrator sources were 70 seconds long. The scheduling algorithm for each set found all combinations of calibrator sources that fell in the elevation ranges and selected the sequence of four objects that minimized the slewing time. The purpose of these observations was 1) to serve as amplitude and bandpass calibrators; 2) to improve robustness of estimates of the path delay in the neutral atmosphere; and 3) to tie positions of new sources to existing catalogues, such as the ICRF catalogue (Ma et al. 1998).

The scheduling algorithm assigned 4 scans for 18% of target sources, 3 scans for 76% sources, 2 scans for 3% sources, and 1 scan for 3% sources. Among 26 objects that were assigned less than 3 scans in a given observing session, 18 were observed in two experiments. During a 24 hour experiment, 11.5–12.0 hours were used for observing target sources, 1.5–2.0 hours for observing calibrators with remaining time was spent slewing.

3 OBSERVATIONS

As mentioned in the introduction, not all of the telescopes in the LBA network are capable of observing in the typical geodetic/astrometric mode of dual S/X frequency bands with multiple spaced subbands and recorded to a Mark5 VLBI system.

HOBART26, PARKES, and DSS45 have a Mark5 recording system and a Mark4 (Whitney et al. 2004) baseband conversion rack. For the first epoch the LBADR system (Phillips et al. 2009) was used, then for all subsequent experiments the Mark5 system was used. Data were recorded onto normal Mark5 diskpacks and shipped to the Max-Plank Institut für Radioastronomie in Bonn for processing.

The ATCA-104, MOPRA and CEDUNA only have the standard LBA VLBI backend consisting of an Australia Telescope National Facility (ATNF) Data Acquisition System (DAS) with an LBADR recorder. The ATNF DAS only allows two simultaneous intermediate frequencies (IFs): either 2 frequencies or 2 polarizations. For each of these IFs the input 64 MHz analog IF is digitally filtered to 2 contiguous 16 MHz bands. ATCA-104, MOPRA, and PARKES have two

Table 2. Observation Summary for each observing session

Telescope	Recorder	Polarization	Frequency Bands (MHz)
Experiment v254b, February 05 2008			
PARKES ATCA-104 MOPRA HOBART26 CEDUNA	LBADR	RCP only	8256–8272 8272–8288 8512–8528 8528–8544
Experiment v271a, August 10 2008			
PARKES HOBART26 DSS45	Mark5	RCP only	8200–8216 8216–8232 8232–8248 8248–8264 8456–8472 8472–8488 8488–8504 8504–8520
CEDUNA	LBADR	RCP only	8200–8216 8216–8232 8456–8472 8472–8488
ATCA-104 MOPRA	LBADR	RCP & LCP	8200–8216 8216–8232 8456–8472 8472–8488
Experiment v271b, November 28 2008			
PARKES HOBART26 DSS45	Mark5	RCP only	8200–8216 8216–8232 8264–8280 8328–8344 8392–8408 8456–8472 8472–8488 8520–8536
CEDUNA	LBADR	RCP only	8200–8216 8216–8232 8456–8472 8472–8488
ATCA-104 MOPRA	LBADR	RCP & LCP	8200–8216 8216–8232 8456–8472 8472–8488
Experiment v271c, July 04 2009			
HOBART26	Mark5	RCP only	8200–8216 8216–8232 8232–8248 8328–8344 8344–8360 8456–8472 8472–8488 8488–8504
PARKES	Mark5 & LBADR	RCP & LCP	8200–8216 8216–8232 8232–8248 8328–8344 8344–8360 8456–8472 8472–8488 8488–8504
CEDUNA	LBADR	RCP only	8200–8216 8216–8232 8456–8472 8472–8488
ATCA-104 MOPRA	LBADR	RCP & LCP	8200–8216 8216–8232 8456–8472 8472–8488

ATNF DAS, however the IF conversion systems at the telescopes means it is impractical to run in any other modes than 2 frequencies and dual polarization. The LBADR data format is not compatible with the Mark4 data processor at Bonn. A custom program was written to translate the data to Mark5B format then it was electronically copied using the Tsunami-UDP application to Bonn, before being copied onto Mark5 diskpacks.

In the last experiment PARKES recorded on the LBADR system in parallel with the Mark5. As this included left circular polarization (LCP) which was not recoded on the Mark5 system and since ATCA-104 and MOPRA recorded both RCP and LCP, the LBADR data were also send to Bonn and LCP correlated against ATCA-104 and MOPRA.

The main limiting factor for frequency selection was the LBADR backend at ATCA-104, MOPRA and CEDUNA where a setup with bands centered on ∼8.2 and∼8.5 GHz was chosen. For the telescopes with Mark5 recorders, the setup was chosen to overlap in frequency with the LBADR setup but also including more frequencies to gain sensitivity. The frequency setup was changed between experiments in order to explore the feasibility to record at 512 Mbit/s at those stations that can support it. The setup for each observing experiment is described in Table 2.

The Australia Telescope Compact Array consists of six 22 metre antennas and may observe as a single antenna or as a phased array of 5 dishes[2]. Since no tests of using a phased ATCA array as an element of the VLBI network for absolute astrometry observations were made before 2010, we decided to use a single dish of the ATCA in order to avoid a risk of introducing unknown systematic errors.

The NASA Deep Space Network station DSS45 observed only 4.5 hours in v271a and 6.5 hours in v271b during intermissions between receiving the telemetry from Mars orbiting spacecraft.

4 CORRELATION

The Bonn Mark4 Correlator was chosen for the correlation of these experiments for two primary reasons. Firstly, the correlator was extensively tested for use in space geodesy and absolute astrometry mode during 2000–2010 and is known to produce highly reliable group delays. Secondly, it was equipped with four Mark5B units and eight Mark5A units, which was a convenient combination since data from three stations were in the Mark5B format (ATCA-104, MOPRA, and CEDUNA) and data from PARKES were in the Mark5B format.

Preparation for correlation required about two months due to complications that arose from the scheduling of different patching and channel outputs (fan out) for use at the stations. The stations that had Mark4 data acquisition racks delivered detailed log files, from which we could reconstruct the channels used, but the LBA stations did not provide log files and the track assignments had to be searched for by trial and error, which was a time-consuming process. The absence of log files also required some custom programming to reconstruct the log VEX file (lvex), which the Mark IV correlator required to perform the correlation. Further, the setup that was chosen was incompatible with the capabilities of the hardware correlator and required an extensive work-around at the correlator.

We chose to correlate with a window of 128 lags (corresponding to a delay window width of 8 mks) instead of the 32 lags (2 mks) normally used for stream correlation to allow for potentially large clock offsets due to instrumental errors and for large a priori source coordinate errors. The integration time was chosen to be as small as possible (0.5 s to 1.0 s) to allow for potentially large residual fringe rates due to source position errors.

The Mark4 correlator can cope with only four stations simultaneously when correlating 128 lags with short integration time. Since the experiment was observed with five

[2] The sixth dish is located at the fixed pad far away from other antennas, which makes its phasing with the rest of the compact array too difficult.

to seven stations in right circular polarization (RCP) and two stations (ATCA-104 and MOPRA) also in left circular polarization (LCP), the correlation had to be split in passes.

As a by-product of the multi-pass correlation, some baselines were correlated more than once and this redundancy was exploited to select the correlation with the best SNR for each duplicated scan. For the LCP correlation, only one pass was required since only the LBA stations recorded the LCP. PARKES recorded LCP only during v271c and this was enabled by the use of two backends (Mark4 and LBA) in parallel. Those stations were re-correlated in a second pass to produce all four polarization products (left-left, right-right, left-right and right-left). For this pass we had to restrict the number of lags to 32 due to correlator hardware constraints, but the integration time was kept at 0.5 s.

Fringe fitting was performed at the correlator using software program FOURFIT, the baseline-based fringe fit offered within the Haystack Observatory Package Software (HOPS) to estimate the residual delay upon which the post-correlation analysis was based. Inspection of fringe-fitted data is a convenient means of data quality control, as one can examine the correlated data on a scan-by-scan basis, looking for problems that might have occurred during correlation or at the stations and permits flagging of bad data immediately.

5 DATA ANALYSIS

The correlator generates the spectrum of the cross-correlation function. The spectrum was processed with the software program FOURFIT that for each scan and each baseline determined phase delay rate, narrow-band delay and wide-band group delay (sometimes also called multi-band delay) that maximized the fringe amplitude. Refer to Takahashi et al. (2000) for a detailed description of the fringe searching process and the distinction between narrow-band and wide-band group delays. The wide-band delay is more precise than narrow-band delay. The formal uncertainties of these delays, σ_n and σ_w are computed by FOURFIT the following way:

$$\begin{aligned} \sigma_n &= \frac{\sqrt{12}}{2\pi\Delta f\,\mathrm{SNR}} \\ \sigma_w &= \frac{1}{2\pi\sigma_f\,\mathrm{SNR}}, \end{aligned} \qquad (1)$$

where Δf the IF bandwidth, σ_f the dispersions of cyclic frequencies across the band, and SNR is the ratio of the fringe amplitude from the wide band fringe search to the rms of the thermal noise. The ratio of σ_w/σ_n was in the range 27–28 for the LCS1 experiments, what gives for observations with typical SNR=30 $\sigma_w \approx 40$ ps and σ_n around one nanosecond.

Among 421 observed targets, 410 were detected. The list of 11 sources that were not detected is shown in Table 3. In addition, 111 calibrators were observed, all of which were detected.

5.1 Data analysis: source position determination

The most challenging part of data analysis was resolving group delay ambiguities. The algorithm of fringe fitting implemented in FOURFIT searches for a global maxima in the Fourier transform of the cross-correlated function averaged over individual IFs after correcting phases for a fringe delay rate and a narrow-band group delay. Fringe spectrum folding results in a rail of maxima of the Fourier transform of the cross-correlated function with exactly the same amplitude and with spacings reciprocal to the minimum difference in IF frequencies. Therefore, the group delay that corresponds to the maxima in the Fourier transform of the cross-correlated function is determined with an ambiguity of $1/2.56 \cdot 10^8$ Hz ≈ 3.9 ns.

It should be noted that typical group delay ambiguity spacings in geodetic observations are in the range 50–200 ns. For successful resolving ambiguities as a rule of thumb the predicted delay should be known with an accuracy better than 1/6 of the ambiguity spacing, 600 ps in our case. This is a challenge. The random errors of the narrow-band group delays are too high for using them directly for resolving ambiguities in wide-band group delays (see Figure 2). In the framework of traditional data analysis of geodetic VLBI observations, the maximum uncertainty in prediction of the path delay is due to a lack of an adequate model for the path delay in the neutral atmosphere. These errors are in the range of 300–2000 ps. The path delay through the ionosphere at 8.3 GHz is in the range 0.03–1.0 nsec. In addition, an error $1''$ in a priori source position — a typical position errors of the AT20G, at the baseline of 1700 km long causes an error in a priori time delay up to 30 ns.

5.1.1 *Group delay ambiguity resolution*

However, it is premature to conclude that resolving group delay ambiguities is impossible. Firstly, we need to use a state-of-the art a priori model. Our computation of theoretical time delays in general follows the approach of Sovers, Fanselow & Jacobs C.S (1998) with some refinements. The most significant ones are the following. The advanced expression for time delay derived by Kopeikin & Schäfer (1999) in the framework of general relativity was used. The displacements caused by the Earth's tides were computed using the numerical values of the generalized Love numbers pre-

Table 3. The list of target sources that were not detected in LCS1 VLBI observations. The last three data columns contain the flux density in mJy extrapolated to 8.3 GHz (F), the spectral index (α), and comment (C). Value -9.99 means the spectral index was not available. Comments: 1) Not in AT20G catalogue; 2) Flagged as an LMC source in AT20G catalogue; 3) Galactic planetary nebula; 4) Flagged as an extended source in AT20G catalogue.

J2000-name	B1950	RA	Dec	F	α	C
J0404−7109	0404−712	04 04 00.99	-71 09 09.7	172	-0.57	1
J0538−6905	0539−691	05 38 45.66	-69 05 03.1	204	-9.99	2
J0552−5349	0551−538	05 52 36.18	-53 49 32.4	182	-0.34	1
J0938−6005	0937−598	09 38 47.20	-60 05 28.7	196	-0.08	3
J0958−5757	0956−577	09 58 02.92	-57 57 42.6	383	0.21	3
J1100−6514	1058−649	11 00 20.09	-65 14 56.4	179	-0.08	3
J1150−5710	1147−569	11 50 17.87	-57 10 56.0	349	0.23	3
J1325−4302	1322−427	13 25 07.35	-43 02 01.8	327	-9.99	4
J1353−6630	1350−662	13 53 57.05	-66 30 50.3	370	0.04	3
J1505−5559	1502−557	15 05 59.17	-55 59 16.2	217	-0.06	3
J1656−4014	1653−401	16 56 47.53	-40 14 24.4	427	-9.99	4

sented by Mathews (2001) following a rigorous algorithm described by Petrov & Ma (2003) with a truncation at a level of 0.05 mm. The displacements caused by ocean loading were computed by convolving the Greens' functions with ocean tide models. The GOT99.2 model of diurnal and semidiurnal ocean tides (Ray 1999), the NAO99 model (Matsumoto, Takanezawa & Ooe 2000) of ocean zonal tides, the equilibrium model (Petrov & Ma 2003) of the pole tide, and the tide with period of 18.6 years were used. Station displacements caused by the atmospheric pressure loading were computed by convolving the Greens' functions that describe the elastic properties of the Earth (Farrell 1972) with the output of the atmosphere NCEP Reanalysis numerical model (Kalnay et al. 1996). The algorithm of computations is described in full detail in Petrov & Boy (2004). The displacements due to loading caused by variations of soil moisture and snow cover in accordance with GLDAS Noah model (Rodell et al. 2004) with a resolution $0.25^\circ \times 0.25^\circ$ were computed using the same technique as the atmospheric pressure loading. The empirical model of harmonic variations in the Earth orientation parameters `heo_20101111` derived from VLBI observations according to the method proposed by Petrov (2007) was used. The time series of UT1 and polar motion derived by the NASA Goddard Space Flight Center operational VLBI solutions were used a priori.

The a priori path delays in the neutral atmosphere in the direction of observed sources were computed by numerical integration of differential equations of wave propagation through the heterogeneous media. The four-dimensional field of the refractivity index distribution was computed using the atmospheric pressure, air temperature and specific humidity taken from the output of the Modern Era Retrospective-Analysis for Research and Applications (MERRA) (Schubert et al. 2008). That model presents the atmospheric parameters at a grid $1/2^\circ \times 2/3^\circ \times 6^h$ at 72 pressure levels.

Secondly, we made a least square (LSQ) solution using narrow-band delay. The positions of all target sources were estimated, as well as clock function for all stations except the one taken as a reference modeled as a sum of the 2nd degree polynomial over the experiment and B-spline of the first order with the time span 60 minutes and residual atmosphere path delay in zenith direction modeled with B-spline of the first order with time span 60 minutes. Constraint on rate of change of clock function and atmosphere path delay were imposed. After the removal of outliers (1–2% of points), the weighted root mean square (wrms) of residuals was 1–4 ns. An example of narrow-band postfit residuals is shown in Figure 2.

The next step was to substitute the adjustments to clock function, atmosphere path delay in zenith direction and source positions from the narrow band LSQ solution to the differences between the wide-band path delays and the theoretical group delays. An example of enhanced wide-band group delays after the substitution and group delay ambiguity resolution is shown in Figure 3.

It is still difficult to resolve ambiguities at long baselines, but relatively easy to resolve the ambiguities at the inner part of the array: ATCA-104, DSS45, MOPRA, PARKES. The group delay ambiguity resolution process starts from the baseline with the least scatter of a priori wide-band delays. After group delay ambiguity resolution at the first

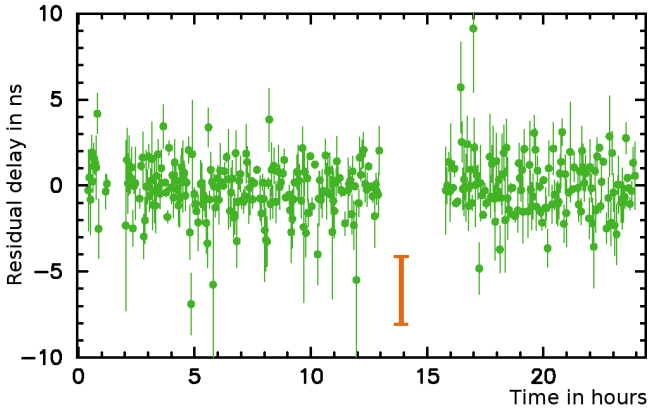

Figure 2. The post-fit residuals of narrow-band group delay LSQ solution at the baseline CEDUNA/HOBART26 in experiment v271a on February 05, 2008. The bar in the middle of the plot corresponds to the ambiguity spacing of the wide-band path group delay.

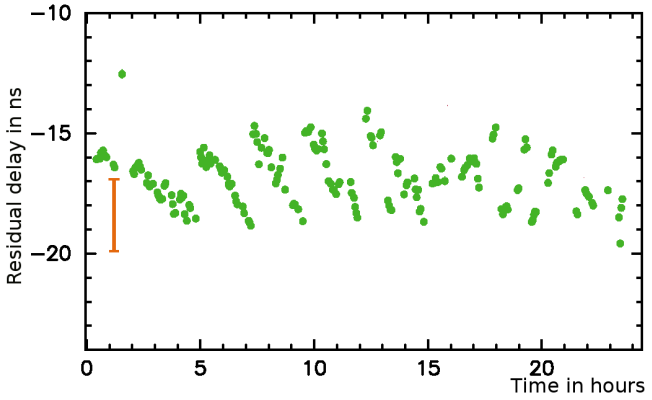

Figure 3. The wide-band a priori group delays after substitution of adjustments to clock function, atmosphere path delay in zenith direction and source positions from the narrow-band LSQ solution at the baseline CEDUNA/PARKES in experiment v271a on February 05, 2008. The bar in the left side of the plot corresponds to the ambiguity spacing of the wide-band path group delay.

baseline and temporary suppression observations with questionable ambiguities, the LSQ solution with mixed delays is made: wide-band group delays at baselines with resolved ambiguities and narrow-band group delays at other baselines. In addition to other parameters, baseline-dependent clock misclosures are estimated.

In the absence of instrumental delays, the differences between wide-band and narrow-band delays would be the zero mean Gaussian random noise. Instrumental delays in the analogue electronics cause systematic changes of these differences in time. Fortunately, these systematic changes are smooth and small enough to allow solving for ambiguities with spacings as small as 3.9 ns. Since the scatter of postfit residual of wide-band group delays is a factor of 10–50 less than the ambiguity spacings, when the instrumental delay is determined, the ambiguities can be resolved. Therefore, the feasibility of resolving wide-band group delays hinges upon the accuracy of determination of the differences between narrow-band and wide-band group delays from analysis of narrow-band delays.

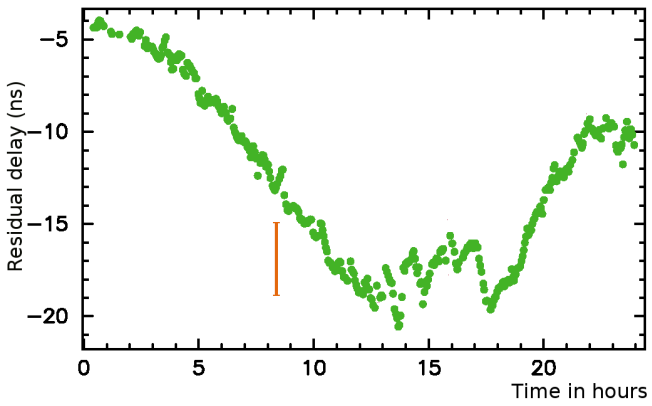

Figure 4. The wide-band a priori group delays at the baseline CEDUNA/PARKES in experiment v271a on February 05, 2008 after substitution of adjustments to clock function, atmosphere path delay in zenith direction from the narrow-band LSQ solution and source positions from the wide-band LSQ solution at other baselines and group delay ambiguity resolution. The bar in the central side of the plot corresponds to the ambiguity spacing of the wide-band path group delay.

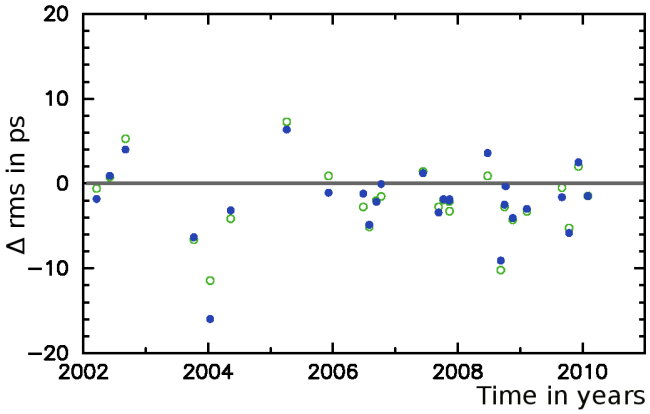

Figure 5. The difference in rms of postfit residuals with respect to the reference dual band X/S solution for two trial solutions: X-band only data (solid discs) and X-band data with ionosphere path delay from GPS TEC map applied (circles).

An example of the a priori wide-band group delay with the substituted adjustments to sources positions found from the wide-band group delay solution at other baselines is shown in Figure 4. After resolving ambiguities for the most of observations, the points that were temporarily suppressed were restored and used in the solution.

5.1.2 Ionosphere path delay contribution

Single band VLBI data are affected by a variable path delay through the ionosphere. We attempted to model this path delay using GPS TEC maps provided by the CODE analysis center for processing Global Navigation Satellite System data (Schaer 1998). Details of computing the VLBI ionospheric path delay using TEC maps from GPS are given in Petrov et al. (2010). The model usually recovers over 80% of the path delay at baselines longer several thousand kilometres. However, applying the ionosphere TEC model to processing LCS1 experiment did not improve the solution and even degraded the fit. The same model and software program certainly improved the fit and improved results when applied to processing observations on intercontinental baselines.

In order to investigate the applicability of the reduction for the path delay in the ionosphere based on GPS TEC maps, we processed 29 IVS dual-band geodetic experiments that included the 1089 km long baseline HOBART26/PARKES. We ran three solutions that included the data only at this baseline. The first reference solution used ionosphere-free linear combinations of X-band and S-band observables. The second solution used X-band only group delays. The third solution used X-band only data and applied the reduction for the path delay in the ionosphere from GPS TEC maps.

We discarded two experiments: one had a clock break at HOBART26 and another had the rms of postfit residual a factor of 5 greater than usually due to a warm receiver. The rms differences of postfit residuals with respect to the reference dual band X/S solution for two trial solutions are shown in Figure 5: one with X-band only data and another with X-band data with ionosphere path delays from GPS TEC map applied. Considering the reference solution based on ionosphere-free group delays as the ground truth, we expected that the rms differences between the X-band only solution (denoted with circles in Figure 5) be positive, and the rms differences of the X-band solution with the ionosphere path delay from GPS TEC maps applied be also positive but less than the rms differences between the X-band only solution. Instead, we see that the rms of postfit residuals of the X-band only solution are *less* than the rms of dial-band reference solution and applying the ionosphere path delay from GPS TEC maps does not affect the rms significantly.

We then computed the rms of the contribution of the ionosphere path delay from dual-band X/S observations and the rms of the differences between the path delay in the ionosphere from the dual-band X/S observations and the GPS TEC ionosphere maps. They are shown in Figure 6. We see that in 2002–2004 the ionosphere path delay from GPS TEC maps was coherent with the dual-band ionosphere path delay estimate. In 2005–2010 the ionosphere path delay was small with rms ∼30 ps and the ionosphere path delay from the GPS TEC model was only partially coherent with the ionosphere path delay estimates from dual-band VLBI observations. The baseline length repeatability, defined as the rms of baseline length estimates after subtraction the secular drift due to tectonics, is the minimum when ionosphere-free linear combinations of X/S observables are used: 17.0 mm, grows to 17.4 mm when X-band group delay are used, and it is the maximum, 18.4 mm, when the ionosphere path delay reduction based on GPS TEC model is applied to X-band observables.

We compared these results with analogous observations in the northern hemisphere. We picked the baseline LA–VLBA/OV–VLBA that has almost exactly the same length as the baseline HOBART26/PARKES: 1088 km against 1089 km. We processed 88 experiments at this baseline in a similar fashion as we processed the HOBART26/PARKES baseline. Results are shown in Figure 7. Applying the ionosphere path delay from GPS has reduced the rms of post-fit residuals at this baseline.

Our interpretation of this phenomena is that the ionosphere path delay from GPS TEC maps at baselines 1–2

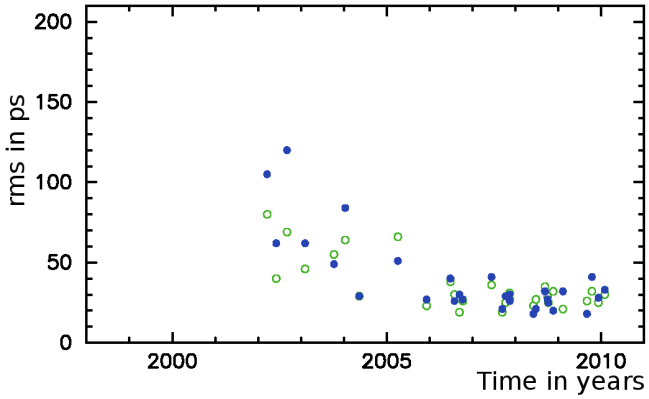

Figure 6. The rms of the ionosphere contribution from dual-band X/S observations (solid disks) and the rms of the differences of the path delay in the ionosphere from the dual-band X/S observations at the baseline HOBART26/PARKES and the GPS TEC ionosphere maps (circles).

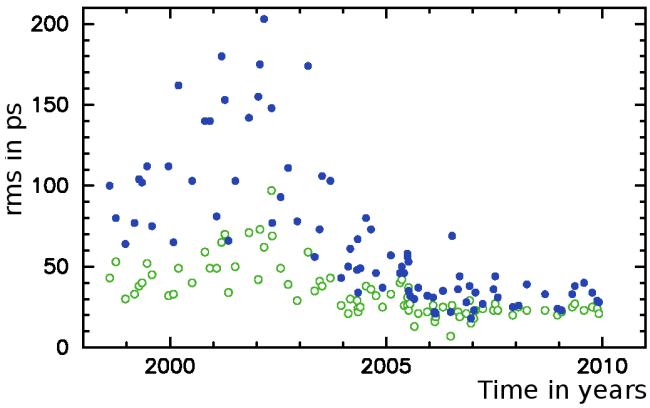

Figure 7. The rms of the ionosphere contribution from dual-band X/S observations (solid disks) and the rms of the differences of the path delay in the ionosphere from the dual-band X/S observations at the 1088 km long baseline LA–VLBA/OV–VLBA and the GPS TEC ionosphere maps (circles).

thousands kilometres has the floor around 30 ps. The dominant constituent in the ionospheric path delay at these scales during the solar minimum are short-periodic scintillations that the GPS TEC model with time resolution 2 hours and the spatial resolution 500 km does not adequately represent. It is also known (Hernández-Pajares et al. 2009) that the accuracy of the GPS TEC model is worse in the southern hemisphere than in the northern hemisphere due to the disparity in the GPS station distribution.

Applying the GPS TEC map ionosphere path delay reduction effectively added noise in the data. Therefore, we did not apply the ionosphere path delay in our final solution.

5.1.3 Re-weighting observations

According to the Gauss-Markov theorem, the estimate of parameters has the minimum dispersion when observation weights are chosen reciprocal to the variance of errors. The group delays used in the analysis have errors due to the thermal noise in fringe phases and due to mismodeling the propagation delay:

$$\sigma^2 = \sigma_{th}^2 + \sigma_{na}^2 + \sigma_{io}^2, \quad (2)$$

where σ_{th} is the variance of the thermal noise, σ_{na}, and σ_{io} are the variances of errors of modeling the path delay in the neutral atmosphere and the ionosphere respectively.

A rigorous analysis of the errors of modeling the path delay in the neutral atmosphere is beyond the scope of this paper. Assuming the dominant error source of the a priori model is the high frequency fluctuations of the water vapor at time scales less than 3–5 hours, we sought a regression model for the dependence of σ_{na}^2 on the non-hydrostatic component of the slanted path delay through the atmosphere. We made several trial runs using all observing sessions under geodesy and absolute astrometry programs for 30 years and added in quadrature to the a priori uncertainties of group delay an additive correction:

$$\sigma_{\rm used}^2 = \sigma_{th}^2 + \left(a \cdot \frac{\tau_s}{\tau_z} \right)^2, \quad (3)$$

where τ_s is the contribution of the non-hydrostatic constituent of the slanted path delay, τ_z is the non-hydrostatic path delay in zenith direction computed by a direct integration of equations of wave propagation through the atmosphere using the refractivity computed using the MERRA model, and a is a coefficient. We found that the baseline length repeatability defined as the rms of the deviation of baseline length with respect to the linear time evolution reaches the minimum when $a = 0.02$. Therefore, we adopted this value our analysis of LCS1 experiments. For a typical values of τ_z, the added noise is 8 ps in zenith direction and 16 ps at the the elevation of 30°.

We computed the rms of ionosphere contributions from dual band VLBI group delays and from GPS TEC maps. Figure 8 shows the dependence of the square of the rms from dual-band VLBI versus the square of the rms from GPS. The slope of the regression straight line is 0.992 ± 0.004. This dependence suggests that although the ionosphere path delay from TEC maps from GPS analysis is too noisy to be applied for reduction of observations at short baselines during the Solar minimum, it correctly predicts *the variance* of the ionosphere path delay. We assigned the variance of the mismodeled ionosphere path delay to the ionosphere contribution to delay computed from TEC maps: $\sigma_{io} = \tau_{io}$.

We also computed for each experiment and for each baseline an ad hoc variances of observables that after being added in quadrature make the ratio of the weighted sum of squares of post-fit residuals to their mathematical expectation close to unity. This computation technique is presented in Petrov et al. (2010). The ad hoc variance was applied to further inflate the formal uncertainties of observable that have already been corrected for the inaccuracy of the a priori model of wave propagation through the ionosphere and neutral atmosphere (expression 2). In contrast to σ_{na}^2 and σ_{io}^2, the baseline-dependent ad hoc variance is elevation independent.

5.1.4 Global LSQ solution

We ran a single global LSQ solution using all available dual-band VLBI observations under geodesy and absolute as-

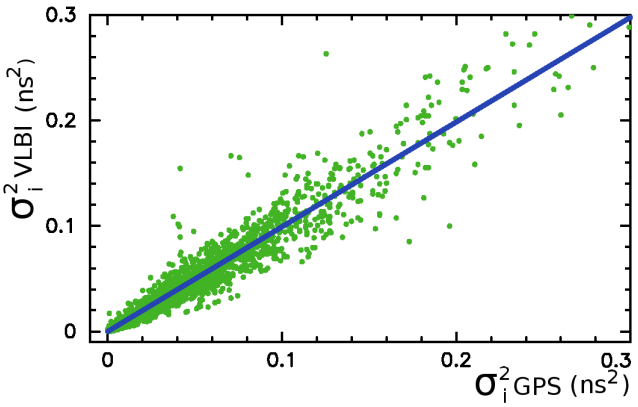

Figure 8. The dependence of the ionosphere path delay σ_i^2 from dual-band VLBI versus σ_i^2 from TEC maps from GPS analysis. Data in time range 2005.0–2010.6 (Solar minimum) were used.

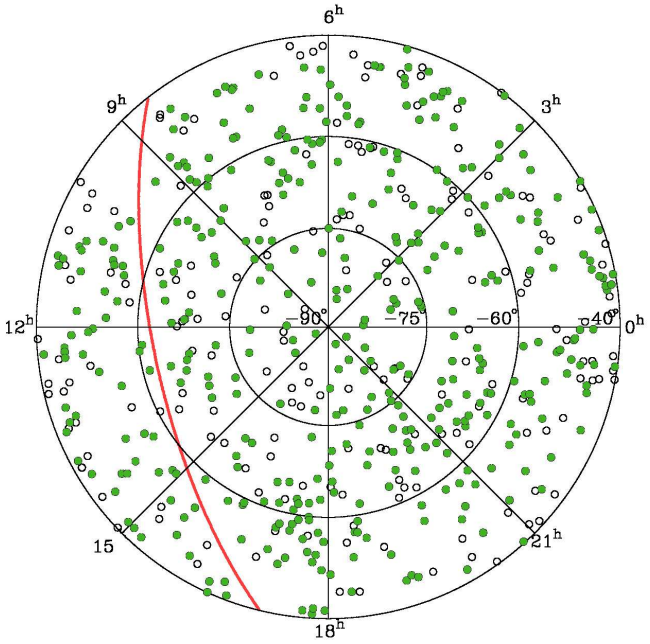

Figure 9. The distribution of sources with milliarcsecond positions at the southern sky. Circles denote sources known by 2008. Filled green discs denote sources from the LCS1 catalogue. The Galactic plane shown by red line.

tronomy observations from 1980.04.12 through 2010.08.04, in total 7.56 million observations, and the X-band VLBI data from 4 LCS1 observing sessions. The RCP and LCP data were treated as independent experiments. The following parameters were estimated over the global dataset: coordinates of 4924 sources, including 410 detected target objects in the LCS1 campaign (see Figure 9); positions and velocities of all stations; coefficients of expansion over the B-spline basis of non-linear motions for 17 stations; coefficients of harmonic site position variations of 48 stations at four frequencies: annual, semi-annual, diurnal, semi-diurnal; and axis offsets for 67 stations. In addition, the following parameters were estimated for each experiment independently: station-dependent clock functions modeled by second order polynomials, baseline-dependent clock offsets, the pole coordinates, UT1-TAI, and daily nutation offset angles. The list of estimated parameters also contained more than 1 million nuisance parameters: coefficients of linear splines that model atmospheric path delay (20 minutes segment) and clock function (60 minutes segment).

The rate of change for the atmospheric path delay and clock function between adjacent segments was constrained to zero with weights reciprocal to $1.1 \cdot 10^{-14}$ and $2 \cdot 10^{-14}$ respectively in order to stabilize our solution. We apply no-net rotation constraints on position of 212 sources marked as "defining" in the ICRF catalogue (Ma et al. 1998) that requires the positions of these source in the new catalogue to have no rotation with respect to the position in the ICRF catalogue.

The global solution sets the orientation of the array with respect to an ensemble of ∼5000 extragalactic remote radio sources. The orientation of that ensemble is defined by the series of the Earth orientation parameters evaluated together with source coordinates. Common 111 sources observed in LCS1 as atmosphere and amplitude calibrators provide strong connection between the new catalogue to the old catalogue of compact sources.

5.2 Error analysis of the LCS1 catalogue

To assess the systematic error in our results we exploited the fact that 111 known sources were observed as amplitude and atmospheric calibrators. Positions of these sources were determined from previous dual-band S/X observations with accuracies better than 0.2 mas. We sorted the set of 111 calibrators according to their right ascensions and split them into two subsets of 55 and 56 objects, even and odd. We ran two additional solutions. In the first solution we suppressed 55 calibrators in all experiments but LCS1 and determined their positions solely from the LCS1 experiment. In the second solution we did the same with the second subset. Considering that the positions of calibrators from numerous S/X observations represent the ground truth, we treated the differences as LCS1 errors.

We computed the χ^2/ndf statistics for the differences in right ascensions and declinations Δ_α and Δ_δ and sought additional variances v_α and v_δ that, being added in quadrature to the formal source position uncertainties, $\sigma_{\alpha,i}$ and $\sigma_{\delta,i}$, make them close to unity:

$$\begin{aligned} \frac{\chi^2_\alpha}{\mathrm{ndf}} &= \frac{\sum \Delta\alpha_i^2 \cos^2\delta_i}{n \sum \sqrt{\sigma^2_{\alpha,i}\cos^2\delta_i + v^2_\alpha}} \\ \frac{\chi^2_\delta}{\mathrm{ndf}} &= \frac{\sum \Delta\delta_i^2}{n \sum \sqrt{\sigma^2_{\delta,i} + v^2_\delta}}. \end{aligned} \qquad (4)$$

We found the following additive corrections of the uncertainties in right ascensions scaled by $\cos\delta$ and for declinations respectively: v_α = 1.44 mas and v_δ=0.51 mas. We do not have an explanation why the additive correction for scaled right ascensions is 3 times greater than for declinations. After applying the additive corrections, the wrms of source position differences are 1.8 mas for right ascension scaled by $\cos\delta$ and 1.5 mas for declinations.

The final inflated errors of source positions, $\sigma^2_\alpha(f)$ and

$\sigma^2_\delta(f)$, are

$$\begin{aligned}\sigma^2_\alpha(f) &= \sigma^2_\alpha + v^2_\alpha/\cos^2\delta \\ \sigma^2_\delta(f) &= \sigma^2_\delta + v^2_\delta.\end{aligned} \quad (5)$$

5.3 Data analysis: correlated flux density determination

Each detected source has from 3 to 60 observations, with the median number of 25. Imaging a source with 25 points at the *uv* plane is a difficult problem, and the dynamic range of such images will be between 1:10 and 1:100, which is far from spectacular. Images produced with the hybrid self-calibration method will be presented in a separate paper. In this study we limited our analysis with mean correlated flux density estimates in three ranges of lengths of the baseline projections onto the plane tangential to the source without inversion of calibrated visibility data. Information about the correlated flux density is needed for evaluation of the required integration time when an object is used as a phase calibrator.

First, we calibrated raw visibilities v for the a priori system temperature T_{sys} and antenna gain $G(e)$: $A_{corr} = v{\cdot}T_{sys}(t,e)/G(e)$. System temperature was measured at each station, each scan. The coefficients of antenna gain expansions into polynomials over elevation angle are presented in Table 4.

At the second step, we adjusted antenna gains using publicly available brightness distributions of calibrator sources made with observations under other programs. We compiled The Database of Brightness Distributions, Correlated Flux Densities and Images of Compact Radio Sources Produced with VLBI[3] from authors who agreed to make their imaging results publicly available. Among 111 sources observed as calibrators, images of 14–27 objects at each experiment were available. These are images in the form of CLEAN components mainly from Ojha et al. (2004, 2005). CLEAN components of source brightness distributions from analysis of the TANAMI program (Ojha et al. 2010) that observed with the LBA concurrently with the LCS1 were not available, but the parameters of one-component Gaussian models that fit the core regions were published. For those sources for which both a set of CLEAN components and the parameter of the Gaussian one-component model were available, we used CLEAN components.

We predicted the correlated flux density F_{corr} for each observation of an amplitude calibrator with known brightness distribution, as

$$\begin{aligned}F_{corr} &= \left|\sum_i c_i e^{\frac{2\pi f}{c}(u\,x+v\,y)}\right| \\ F_{corr} &= S\,e^{\frac{\pi^2}{4\ln 2}(a^2(u\cos\theta+v\sin\theta)^2+b^2(-u\sin\theta+v\cos\theta)^2)},\end{aligned} \quad (6)$$

where c_i is the correlated flux density of the ith CLEAN component with coordinates x and y with respect to the center of the image; u and v are the projections of the baseline vectors on the tangential plane of the source; and a and b are the FWHM of the Gaussian that approximates the core, and θ is the position angle of the semi-major axis of the Gaussian model.

[3] Available at `http://astrogeo.org/vlbi_images`

Then we built a system of least square equations for all observations of calibrators with known images used in astrometric solutions:

$$F_{corr} = \sqrt{g_i\,g_j}A_{corr} \quad (7)$$

and after taking logarithms from left and right hand sides solved for corrections to gains g for all stations. Finally, we applied corrections to gain for observations of all other sources.

The correlated flux density is a constant during observing session only for unresolved sources. For resolved sources the correlated flux density depends on the projection of the baseline vector on the source plane and on its orientation. We binned the correlated flux densities in three ranges of the baseline vector projection lengths, 0–6 Mλ, 6–25 Mλ, 25–50 Mλ, and found the median value within each bin. These bins correspond to scales of the detected emission at > 30 mas, 7–30 mas, and < 7 mas respectively.

The errors of our estimates of the correlated density depend on the thermal noise described as $\sigma_{th} = F_{corr}/\mathrm{SNR}$ and errors of gain calibration. The variance of the thermal noise was in the range of 1 to 6 mJy depending on the sensitivity of a baseline, with the median value of 3 mJy. The LSQ solution for gains provided the variance of the logarithm of gains. Assuming the calibration errors to be multiplicative in the form $g\,(1+\epsilon)$, where g is gain, we can evaluate the variance of calibration errors as

$$\sigma_c = F_{corr} \times \exp\left(\tfrac{1}{2}\sqrt{\mathrm{Cov}(s_1,s_1)+\mathrm{Cov}(s_2,s_2)+2\,\mathrm{Cov}(s_1,s_2)}\right),$$

where $\mathrm{Cov}\,s_i, s_j$ is the covariance of the logarithm of gain between the i-th and j-th station. Multiplicative gain errors are in the range 0.08–0.1 for DSS45 and 0.02–0.05 for other stations. Gain errors of DSS45 are greater, because it observed 3–5 times less than other stations. The total variance is a sum in quadrature of σ_c and σ_{th}. We should note that our estimate of systematic errors does not account for possible errors in gain curve determination. A systematic error in the gain curve would directly affect our estimate of the correlated flux density. It will also affect the maps of calibrators sources that we took from literature, and thus indirectly affect our estimates of gain corrections. We do not have information about errors of gain curves of LBA antennas.

Table 5 displays 12 out of 633 rows of the catalogue of correlated flux density estimates. The full table is available in the electronic attachment. Column 1 and 2 contain the J2000 and B1950 IAU names of a source; column 3 contains the observation date of the experiment; the 4th column contains the status of the source: `Cal` if it was used as amplitude calibrator; the 5th columns contains the number of RCP observations used in processing. Columns 6, 7, and 8 contain median values of correlated flux densities determined in that experiment at baseline projection lengths 0–6 $M\lambda$, 6–25 $M\lambda$, and 25–50 $M\lambda$ respectively. Columns 9, 10, and 11 contain the arithmetic mean of correlated flux density errors that accounts for both thermal noise and uncertainties in calibration. If no data were collected to that range of baseline projection lengths, -1.0 is used as a substitute. Column 12 contains the experiment name.

Figure 10 shows the probability density histogram of correlated flux densities in LCS1 experiments.

Table 4. The coefficients of antenna gain polynomials over elevation angle expressed in radians. Gain = DPFU $\sum_{k=0}^{k=5} a_k E^k$. The DPFU is shown in the second columns. Columns 3–8 hold coefficients of degree 0 through 5.

Station	DFPU K/Jy	The coefficients of polynomial for gain as a function of the elevation angle in degrees					
		0	1	2	3	4	5
ATCA-104	0.100	1.0	0.0	0.0	0.0	0.0	0.0
CEDUNA	1.000	0.9045	$4.032 \cdot 10^{-3}$	$-4.280 \cdot 10^{-5}$	0.0	0.0	0.0
DSS45	0.240	0.9700	$2.927 \cdot 10^{-3}$	$-1.070 \cdot 10^{-4}$	$1.761 \cdot 10^{-6}$	$-1.112 \cdot 10^{-8}$	0.0
HOBART26	0.058	0.6997	$4.445 \cdot 10^{-2}$	$-2.331 \cdot 10^{-3}$	$5.335 \cdot 10^{-5}$	$-5.412 \cdot 10^{-7}$	$1.926 \cdot 10^{-9}$
MOPRA	0.095	1.0	0.0	0.0	0.0	0.0	0.0
PARKES	0.480	0.7900	$3.368 \cdot 10^{-3}$	$8.507 \cdot 10^{-5}$	$-1.398 \cdot 10^{-6}$	0.0	0.0

Table 5. The first 12 rows of the catalogue of source correlated flux density estimates for both 410 target sources and 111 calibrator sources in each experiment. Some sources were observed on more than one experiment. The table columns are explained in the text. The full table is available in the electronic attachment.

J2000-name	B1950-name	Date	Sts	# Obs	Corr. flux density (Jy)			Flux density error (Jy)			Exp
J0004−4736	0002−478	2008.11.28		12	0.352	0.268	0.267	0.015	0.019	0.013	v271b
J0011−8443	0009−850	2008.02.05		30	0.161	0.165	0.180	0.005	0.005	0.006	v254b
J0012−3954	0010−401	2008.02.05		16	0.761	0.769	0.715	0.016	0.012	0.014	v254b
J0012−3954	0010−401	2009.07.04	Cal	10	0.815	0.654	0.640	0.026	0.023	0.028	v271c
J0028−7045	0026−710	2008.11.28		40	0.092	0.086	0.081	0.005	0.006	0.005	v271b
J0030−4224	0027−426	2009.07.04		30	0.312	0.290	0.256	0.011	0.010	0.011	v271c
J0033−4236	0031−428	2009.07.04		30	0.132	0.135	0.143	0.005	0.005	0.008	v271c
J0034−4116	0031−415	2009.07.04		18	0.053	0.045	0.039	0.003	0.002	0.004	v271c
J0040−4253	0038−431	2009.07.04		28	0.068	0.058	0.067	0.003	0.002	0.007	v271c
J0042−4030	0039−407	2009.07.04		26	0.255	0.253	0.276	0.010	0.011	0.013	v271c
J0042−4333	0040−438	2009.07.04		30	0.165	0.113	0.126	0.005	0.005	0.008	v271c
J0044−8422	0044−846	2008.02.05		26	0.278	0.255	0.234	0.007	0.006	0.007	v254b

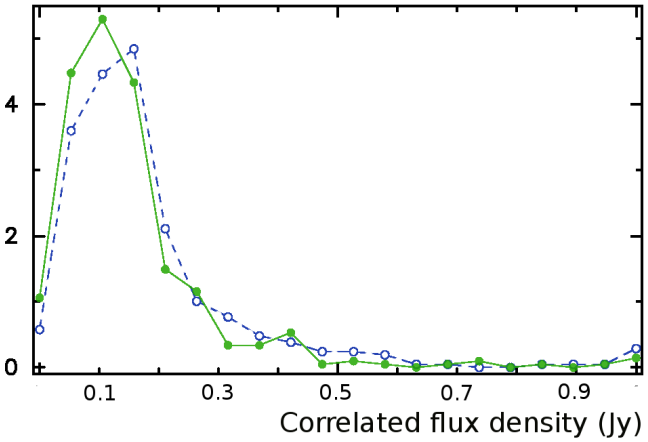

Figure 10. The probability density histogram of correlated flux densities in LCS1 experiments. The dotted line with dicks denotes correlated flux densities at baseline projection lengths 0–6 Mλ, the solid line with discs denotes the correlated flux density at projection lengths 25–50 Mλ,

6 THE LCS1 CATALOGUE

Table 6 displays 12 out of 410 rows of the LCS1 catalogue of source positions. The full table is available in the electronic attachment. Column 1 and 2 contain the J2000 and B1950 IAU names of a source; column 3, 4, and 5 contain hours, minutes and seconds of the right ascension; columns 6, 7, 8 contain degrees, minutes and arcseconds of declination. Columns 9 and 10 contain inflated position errors in right ascension (without multiplier $\cos\delta$) and declination. Column 11 contains correlation coefficient between right ascension and declination, column 12 contains the total number of observations used in position data analysis including RCP and LCP data. Columns 13, 14, and 15 contain the median estimates of the correlated flux density over all experiment of the source in three ranges of baseline projection lengths: 0–6 $M\lambda$, 6–25 $M\lambda$, and 25–50 $M\lambda$. Columns 16, 17, and 18 contain estimates of correlated flux density errors.

Of 421 sources observed, 410 were detected in three or more scans. In four LCS1 observing sessions, 17,731 observations out of 19,494 were used in the LSQ solution together with 7.56 million of other VLBI observations. The semi-major error ellipse of inflated position errors varies in the range 1.4 to 16.8 mas with the median value of 2.6 mas. The distribution of sources on the sky is presented in Figure 9. The histogram of position errors is shown in Figure 11.

7 SUMMARY

The absolute astrometry LBA observations turned out highly successful. The overall detection rate was 97% — the highest rate ever achieved in a VLBI survey. If we exclude extended sources, non-AT20G sources and the 6 planetary nebulae picked in the candidate list due our oversight, the detection rate is 99.8%! We attribute this high detection

Table 6. The first 12 rows of the LCS1 catalogue of source positions of 410 target sources. The table columns are explained in the text. The full table is available in the electronic attachment.

J2000-name	B1950-name	Right ascension	Declination	(9)	(10)	(11)	(12)	(13)	(14)	(15)	(16)	(17)	(18)
J0011−8443	0009−850	00 11 45.90267	−84 43 20.0096	46.1	3.1	-0.228	30	0.162	0.165	0.180	0.005	0.005	0.006
J0028−7045	0026−710	00 28 41.56281	−70 45 15.9267	7.1	1.7	0.006	40	0.092	0.086	0.081	0.005	0.006	0.005
J0030−4224	0027−426	00 30 17.49264	−42 24 46.4827	2.0	1.4	-0.036	37	0.312	0.290	0.256	0.011	0.010	0.011
J0033−4236	0031−428	00 33 47.94145	−42 36 14.0676	3.7	2.2	-0.012	37	0.132	0.135	0.143	0.005	0.005	0.008
J0034−4116	0031−415	00 34 04.40893	−41 16 19.4729	7.1	3.6	0.089	25	0.053	0.045	0.039	0.003	0.002	0.004
J0040−4253	0038−431	00 40 32.51473	−42 53 11.3916	4.5	2.8	0.057	35	0.068	0.058	0.067	0.003	0.002	0.007
J0042−4030	0039−407	00 42 01.22481	−40 30 39.7419	3.4	2.0	0.013	33	0.255	0.253	0.276	0.010	0.011	0.013
J0042−4333	0040−438	00 42 24.86725	−43 33 39.8164	3.9	2.3	0.002	37	0.165	0.113	0.126	0.005	0.005	0.008
J0044−8422	0044−846	00 44 26.68719	−84 22 39.9895	44.0	2.9	-0.237	30	0.278	0.255	0.234	0.007	0.006	0.007
J0047−7530	0046−757	00 47 40.81228	−75 30 11.3640	6.4	1.4	-0.631	41	0.139	0.118	0.078	0.006	0.008	0.006
J0049−4457	0046−452	00 49 16.62412	−44 57 11.1658	3.7	2.1	-0.005	37	0.244	0.215	0.207	0.009	0.006	0.011
J0054−7534	0052−758	00 54 05.81337	−75 34 03.6325	6.3	1.4	-0.803	44	0.094	0.087	0.080	0.004	0.007	0.006

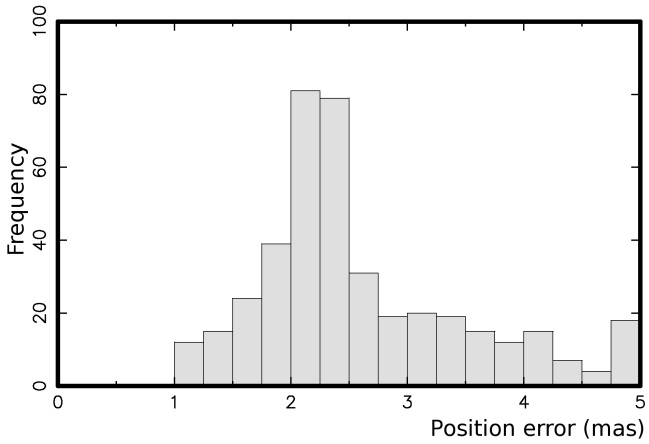

Figure 11. The histogram of the semi-major axes of inflated position error ellipses among 410 sources in the LCS1 catalogue.

rate to two factors. Firstly, the AT20G catalogue is highly reliable and is biased towards to highly compact objects. Selecting candidates based on simultaneous AT20G spectral index proves to be a good methodology. Secondly, the LBA has very high sensitivity. The baseline detection limit over 2 minute of integration time varied from 7 mJy to 30 mJy, with 7–12 mJy at baselines with PARKES.

We have successfully resolved group delay ambiguities with spacing 3.9 ns for all observations. This became possible using the innovative algorithm exploiting relatively low level of instrumental group delay errors.

We have determined positions of 410 target sources never before observed using VLBI with the median uncertainty 2.6 mas. Error analysis showed a moderate contribution of the mismodeled ionosphere path delay to the overall error budget. Both random and systematic errors are accounted for in the error ascribed to source positions exploiting the overlap of 111 additional sources observed in LCS1 experiments with their positions known from prior observations. The positional accuracy of the LCS1 catalogue is a factor of 350 greater than the positional accuracy of the AT20G catalogue which corresponds to the ratio of the maximum baselines of the LBA and the ATCA. The new catalogue has increased the number of sources with declinations $< -40^\circ$ from 158 to 568, i.e. by a factor of 3.5.

We determined correlated flux densities for 410 target and 111 calibrator sources and presented their median values in three ranges of baseline projection lengths. The correlated flux density of target sources varied from 0.02 to 2.5 Jy, being in the range of 80–300 mJy for 70% sources. Errors of the correlated flux densities were estimated to be in the range of 5–8% for the most of the sources.

This observing program is continuing. By November 2010, four additional twenty four hour experiments were observed with several more observing sessions planned.

8 ACKNOWLEDGMENTS

The authors made use of the database CATS of the Special Astrophysical Observatory. We used in our work the dataset MAI6NPANA provided by the NASA/Global Modeling and Assimilation Office (GMAO) in the framework of the MERRA atmospheric reanalysis project. The Long Baseline Array is part of the Australia Telescope National Facility which is funded by the Commonwealth of Australia for operation as a National Facility managed by CSIRO.

REFERENCES

Beasley A. J., Gordon D., Peck A. B., Petrov L., MacMillan D. S., Fomalont E. B., Ma C., 2002, ApJS, 141, 13
Cohen M. H. & Shaffer D. B., 1971, AJ, 76, 91.
Deller A. T., Tingay S. J., Bailes M., Reynolds J. E., 2009, ApJ, 701, 1234
Eichhorn G. et al. 2002, Ap&SS, 282, 299
Farrell W. E., 1972, Rev. Geophys. and Spac. Phys., 10(3), 751
Fey A. et al., 2004, AJ, 127, 1791
Fey A. et al., 2006, AJ, 132, 1944
Fomalont E., Petrov L., McMillan D. S., Gordon D., Ma C. 2003, AJ, 126, 2562
Hernández-Pajares M. et al., 2009, Jour. Geodesy, 83, 263
Kalnay E. M. et al., 1996, Bull. Amer. Meteorol. Soc., 77, 437–471
Kopeikin S. M. & Schäfer G., 1999, Phys Rev D, 60(12), 124002
Kovalev Y.Y., Petrov L., Fomalont E., Gordon D., 2007, AJ, 133, 1236

Lanyi G. E. et al., 2010, AJ, 139, 1695
Ma C. et al., 1998, AJ, 116, 516
Massardi M. et al., 2010, MNRAS, in press, preprint (astro-ph/1010.5942)
Mathews P.M., 2001, J Geod Soc Japan, 47(1), 231–236
Matsumoto K., Takanezawa T., Ooe M., 2000, J Oceanography, 56, 567–581
Matveenko L. I., Kardashev N. S., Sholomitskii G. B., 1965, Izvestia VUZov. Radiofizika, 8, 651 (English transl. Soviet Radiophys., 8, 461)
Murphy T. et al., 2010, MNRAS, 420, 2403
Ojha R. et al., 2004, AJ, 127(6), 3609
Ojha R. et al., 2005, AJ, 130, 2529
Ojha R. et al., 2010, A&A, 519, A45
Petrov L., 2007, A&A, 467(1), 359
Petrov L., Ma C., 2003, J Geophys Res, 108(B4), 2190
Petrov L., Boy J.-P., 2004, J Geophys Res, 109, B03405
Petrov L., Kovalev Y.Y., Fomalont E., Gordon D., 2005, AJ, 129, 1163
Petrov L., Kovalev Y.Y., Fomalont E., Gordon D., 2006, AJ, 131, 1872
Petrov L., Kovalev Y.Y., Fomalont E., Gordon D., 2007, AJ, 136, 580
Petrov L., Hirota T., Honma M., Shibata S. M., Jike T. , Kobayashi H., 2007, AJ, 133, 2487
Petrov L., C. Phillips, A. Bertarini, A. Deller, S. Pogrebenko, A. Mujunen, 2009, PASA, 26(1), 75
Petrov L., Gordon D., Gipson G., MacMillan D., Ma C., Fomalont E., Walker R. C., Carabajal C., 2009, Jour. Geodesy, 83(9), 859
Petrov L., Kovalev Y.Y., Fomalont E., Gordon D., 2010, preprint (astro-ph/xxxxxx)
Phillips C., Tzioumis T., Tingay S., Stevens J., Lovell J., Amy S., West C., Dodson R., 2009, in Proc. Science and Technology of Long Baseline Real-Time Interferometry The 8th International e-VLBI Workshop, EXPReS09, 99 (http://pos.sissa.it/cgi-bin/reader/ conf.cgi?confid=82)
Ray R.D., 1999, NASA/TM-1999-209478, Greenbelt, MD USA
Rodell M., et al., 2004, Bull. Amer. Meteor. Soc., 85(3), 381
Ros E., Marcaide J. M., Guirado J. C., Sardón E., Shapiro I. I., 2000, A&A, 356, 357
Schubert S., et al., In Proc. of Third WCRP International Conference on Reanalysis, Tokyo, 2008, V1–104 (http://wcrp.ipsl.jussieu.fr/Workshops/Reanalysis2008/Documents/V1-104_ea.pdf)
Sekido, M., Kondo, T., Kawai, E., Imae, M., 2003, Rad. Sci., 38(4), 8
Sovers O. J., Fanselow J. L., Jacobs C. S., 1998, Rev Modern Phys, 70(4), 1393–1454
Schaer S., 1998, PhD thesis, Univer. Bern (ftp://ftp.unibe.ch/aiub/papers/ionodiss.ps.gz)
Takahashi F., Kondo R., Takahashi Y., Koyama Y., 2000, Very long baseline interferometer, Ohmsha, Ltd, Tokyo
Verkhodanov O. V., Trushkin S. A., Andernach H., & Chernenkov V. N., 1997, in G. Hunt, & H. E. Payne, eds., ASP Conf. Ser. 125, Astronomical Data Analysis Software and Systems VI, p. 322
Whitney A. R. et al., 2004, Radio Sci, 39, RS1007
Wrobel J., 2009, NRAO eNews, 2(11), 6 (http://www.nrao.edu/news/newsletters/enews/enews_2_11/enews_2_11.pdf)